Constructing TiO$_2$ nanoparticles patched nanorods heterostructure for efficient photodegradation of multiple organics and H$_2$ production

Dongsheng Hu [a], Yu Xie [a,*], Lianjun Liu [b,*], Panpan Zhou [a], Jie Zhao [a], Jiangwei Xu [a], Yun Ling [a]

[a] Nanchang Hangkong University, Department of Material Chemistry, Nanchang, Jiangxi Province, China
[b] University of Wisconsin-Milwaukee, Mechanical Engineering Department, Milwaukee, WI, USA

ABSTRACT

Morphology and exposed facets controlled synthesis of TiO$_2$ has attracted numerous interests due to their fascinating shape-dependent photocatalytic activity, while it still remains in a great challenge to construct TiO$_2$ nanocrystals with surface heterojunction. Here we innovatively constructed a heterostructure of TiO$_2$ nanoparticles patched nanorods (i.e., NP/NR), where the NP and NR were predominately enclosed with the {101} and {100} facets, respectively. Since the highly dispersed nanoparticles (smaller than 10 nm) were closely contacted with nanorods and their electronic band structures are mismatched, it is very likely to form a NP-{101}/NR-{100} surface heterojunction, which significantly facilitates the charge separation and transfer. The ratio of NP to NR is an important factor to govern the NP dispersion, the contact with NR, and the charge separation efficiency, thus determining their photocatalytic activity. Compared with the NP and NR alone, NP$_{0.5}$/NR$_{0.5}$ has the optimum ratio and shows an excellent cycling capability for methyl orange degradation (99% retention over 6 cycles) and superior activity for both the photodegradation of multiple organics (2 times faster) and water splitting to H$_2$ (over 10 times enhancement). A possible charge transfer mechanism on NP-{101}/NR-{100} surface heterojunction has also been proposed to understand the relationship between materials structure and performance. Together with the mechanism study, the nanostructure innovation will advance the development of functional materials for renewable energy and sustainable environment.

© 2016 Elsevier B.V. All rights reserved.

1. Introduction

Titanium dioxide (TiO$_2$), particularly in anatase phase, has been widely used as photocatalysts for photodegradation of organic compounds in water, photocatalytic water splitting to H$_2$, dye-sensitized solar cells, and artificial photosynthesis of solar fuels from CO$_2$ [1–4]. However, using TiO$_2$ as photocatalysts often suffers from a hurdle of low quantum efficiency (QE) primarily because of the fast electron-hole recombination rate and limited harvesting of visible light (caused by its wide band gap, 3.2 eV). Towards these challenges, a number of studies have been conducted to modify TiO$_2$ properties either to enhance charge transfer or extend visible light response, including depositing noble metal (e.g., Pt) or oxides (e.g., Fe$_2$O$_3$) [5,6], doping nonmetal (e.g., N. S) or ions (e.g., Mn^{4+}, Cu^{2+}) [7–11], coupling with quantum dot sensitizers (e.g., CdS)

[12,13], and incorporating with electron carrier (e.g., graphene) [14–16].

Beside above strategies of introducing external elements on TiO$_2$, engineering TiO$_2$ itself with novel nanostructures is an alternative way to improve the QE [4,17,18]. It has been established that the intrinsic properties of anatase TiO$_2$ depended on the shapes, sizes and especially the exposed facets [19,20]. Accordingly, extensive attention has been paid to controllably synthesize TiO$_2$ nanostructures with various morphologies (e.g., nanotubes, nanorods, nanowires, nanosheets), tuneable sizes (e.g., nanosize, microsize), and specific exposed facets (e.g., {101}, {001}, {100}, {110}) [2–4,17]. For example, the exposure of high surface energy {001} facets in TiO$_2$ nanosheets could provide additional adsorption sites, superior electronic band structure, and unsaturated 5-coordinated Ti atoms, thus leading to a higher photocatalytic activity than the low surface energy {101} facets [20–23].

Constructing TiO$_2$ heterojunction is also a promising way to tackle the obstacles in TiO$_2$ to enhance the QE. As known, TiO$_2$ has three typical crystal phases, i.e., anatase, rutile, and brookite, while building TiO$_2$ phase-junctions (e.g., anatase/rutile, rutile/brookite

and anatase/brookite) has demonstrated to facilitate the charge transfer from one phase to another (e.g., electron migration from anatase to rutile) [24–29]. As a result, TiO_2 in the mixed phase exhibited a higher activity than the single phase. Recently, a few studies have demonstrated the formation of surface heterojunction (e.g., {001}/{101}) within one nanosheet or nanocube, because the Fermi level of {001} facets enters their valence band while that of {101} facets is still on the top of their valence band [30–32]. The {001}/{101} heterojunction could facilitate the separation and transfer of electron-hole pairs on the different facets, thus inducing higher activity than the {001} and {101} alone, largely dependent on the ratio of {001} to {101}. This promising {001}/{101} nanocrystals have been applied for CO_2 photoreduction to CH_4 and photodegradation of methyl orange or Rhodamine B [30–33]. Despite of the advantages of TiO_2 {001}/{101} surface heterojunction, the materials were usually synthesized from toxic precursor (TiF_4) or using corrosive HF agent and organic capping agent or by a complex method. Till now, except {001}/{101} no other new surface heterojunctions (such as {100}/{101}) have been reported, even though theoretical calculations suggested that anatase {100} facets are more active than {001} and {101} facets [34,35]. Especially synthesis of {100}/{101} surface heterojunction in a facile and green route still remains in a big challenge. It hence requires comprehensive exploration on this promising but seldom studied {100}/{101} heterojunction.

To prove our new concept of {100}/{101} heterojunction, herein, we report a simple hydrothermal method to construct a novel architecture of TiO_2 nanoparticles patched nanorods with tuneable ratio, where the nanoparticles and nanorods are dominated with {101} and {100} exposed facets, respectively. We hypothesize that (1) nanorods can act as matrices where nanoparticles could be highly dispersed, thus forming a rough surface that increases the porosity and surface area, and (2) the close contact and band structure alignment between nanoparticles and nanorods could form {100}/{101} surface heterojunction, which inhibits the recombination of charge carriers. The outstanding performance of this heterostructured TiO_2 NP/NR for photocatalytic degradation of multiple organics and H_2 production is hence expected. To the best of our knowledge, this is for the first time to fabricate such multifunctional heterojunction especially for water treatment and splitting. In addition to materials structure innovation, another novelty of this work is to prepare the materials in an environmental friendly route without F^--containing chemicals. We also tentatively approach the charge transfer mechanism between {100} and {101} facets.

2. Experimental

2.1. Chemicals

The chemicals used for materials synthesis are TiO_2(P25) (Beijing Entrepreneur Science & Trading Co., Ltd.), sodium hydroxide (NaOH, >96.0%, West Long Chemical Co.), isopropyl alcohol (IPA), titanium (IV) isopropoxide (TIP; 97%, New Chemical Materials Co., Ltd., Shanghai Code), diethylenetriamine (DETA; 99%, Shanghai Biochemical Co., Macklin), ethanol (>96.0%), and deionized water (a Milli Q system with an electrical resistance of 18.4 MΩ cm).

2.2. Materials preparation

TiO_2 nanorods were prepared by a hydrothermal method as reported elsewhere [19]. Briefly, 2 g P25 and 80 ml of 10 M NaOH aqueous solution were mixed and transferred to a 100 ml Teflon-lined stainless steel autoclave. The autoclave was put into an oven and heated at 200 °C for 24 h. After cool down to room temperature

naturally, the white precipitates (Na-titanates) were collected by centrifugation and washed with deionized water till the pH 10.5. After that, 1 g Na-titanates were re-dispersed into 40 ml deionized water and transferred to a 50 ml Teflon-lined stainless steel autoclave. The autoclave was heated at 200 °C for 24 h in an oven. The final white precipitates (i.e., nanorods) were collected by washing and drying at 60 °C in vacuum for 10 h.

TiO_2 microspheres, composed of nanoparticles, were prepared by a solvothermal method [36]. In brief, 1.25 ml TIP, 0.2 ml DETA and 70 ml IPA were mixed in a beaker and thoroughly ultrasonicated for 30 min. Then the solution was transferred into 100 ml Teflon-lined stainless steel autoclave and kept in an electric oven at 200 °C for 24 h. After cool down to room temperature, the white precipitate was harvested via centrifugation, washed thoroughly with ethanol, and dried at 60 °C overnight.

TiO_2 nanoparticles patched TiO_2 nanorods heterostructures were prepared by a solvothermal method. Typically, a desired amount of nanorods were re-dispersed in 70 ml IPA and ultrasonicated for 30 min to ensure the powder well dispersed. Next, a certain amount of TIP and 0.2 ml DETA were added into the IPA solution. After vigorously stirring for 30 min, the solution was transferred into 100 ml Teflon-lined stainless steel autoclave. The same procedures as the preparation of TiO_2 particles were then conducted to treat the heterostructure precipitates. All of the nanorods, microspheres, and the mixed nanoparticles/nanorods products were calcined at 400 °C for 2 h. Through adjusting the amount of TIP, we controllably prepared nanoparticles patched nanorods with different weight ratio, i.e., 25%/75%, 50%/50%, and 75%/25%. The final products were denoted as NR, $NP_{0.25}/NR_{0.75}$, $NP_{0.5}/NR_{0.5}$, $NP_{0.75}/NR_{0.25}$, and NP, where NR and NP refer to pure nanorods and nanoparticles, respectively.

2.3. Materials characterization

X-ray diffraction (XRD, Rigaku, RINT 2000) was carried out to investigate the crystal phase with monochromated high intensity CuKα radiation (λ = 0.15418 Å) in the 2θ range of 5–80°. Raman spectra were obtained on a laser Raman spectrometer with a back scattering con-figuration using an Ar + laser (20 mW, 532 nm) as excitation source. The surface composition and chemical state were analyzed by X-ray photoelectron spectroscopy (XPS). Measurements were carried out on an X-ray photoelectron spectrometer (ESCALAB MK II) using MgKa (1253.6 eV) X-rays as the excitation source and C 1s (284.6 eV) for calibration. Valence band (VB) XPS spectra for TiO_2-based heterostructures were also taken using the same XPS system. Measurements were performed using an ultra-high vacuum chamber with a base pressure below 5×10^{-9} Torr. The VB spectra were recorded in the binding energy range from −5 to 20 eV with analyzer pass energy of 20 eV and step size of 0.1 eV. The morphology of the as-synthesized samples was characterized by Field-emission scanning electron microscopy (FESEM) using JSM-6700F in a secondary electron scattering mode at 15 kV. The morphology and lattice structure was examined using transmission electron microscopy (TEM, Tecnai G2F20 S-Twin) that was operated with accelerating voltage of 200 kV. The surface area and porosity of the materials were examined by N_2 adsorption/desorption at 77 K using the Brunauer–Emmett–Teller (BET) method (Micromeritics, ASAP 2020). To determine the band gap of the materials, ultraviolet–visible (UV–vis) diffusion reflectance spectra were collected on a Solid Spec-3700DUV spectrophotometer (Shimadzu) using $BaSO_4$ as background.

2.4. Photocatalytic activity measurement

The degradation of multiple organic compounds, such as Methyl orange, Methylene Blue, Rhodamine B, Malachite Green, and

Bisphenol A, has been conducted over the as-synthesized TiO_2 materials under UV–vis light. A 300 W Xe lamp (PLS-SXE300, Perfect Light Company, Beijing, China) was used as light source, and the light intensity was 100 mW/cm^2. Prior to photo-degradation, 50 mg of photocatalyst was added into the organic solution (50 ml, 10 mg/l), ultrasonicated for 5 min, and then stirred for 30 min in the dark to ensure the well dispersion and the full contact between the photocatalysts and the organic molecules [37]. In this case, the organic compounds could reach adsorption–desorption equilibration. After that, the light was turned on for irradiation for 120 min. At each 20 min, 3 ml solution was collected. The photocatalyst was separated by centrifugation, and the concentration of residual organics in the solution was measured by UV–vis spectrophotometer (UV-2550, Shimadzu, Japan).

Photocatalytic water splitting to H_2 was carried out in a double jacketed British purple glass reactor (Labsolar-H_2, Perfect Light Company, China). The reactor has a flat optical window on the top, allowing for the light irradiation and penetration. On the side of the reactor is a cooling water system. The reactor is also connected with a vacuum pump, which is used to remove the air in the system. A 300 W Xe lamp (PLS-SXE300, Perfect Light Company, China) was used as light source. 50 mg of photocatalyst was dispersed in 80 ml solution that contains 10% methanol as sacrificial reagent. Prior to the reaction, the solution was stirred thoroughly to ensure the photocatalyst well dispersed. The reaction was conducted in a closed system continuously for 4 h. The amount of H_2 evolution was measured using a gas chromatography (GC) with thermal conductivity detector (TCD, Huaai GC9560, China).

2.5. Photocurrent measurement

The photocurrent was measured on CHI660D electrochemical workstation by using a standard three-electrode system. A graphite electrode, standard calomel electrode in saturated KCl and the as-prepared TiO_2 were used as the counter electrode, reference electrode, and working electrode, respectively. 0.5 M sodium sulfate was used as the electrolyte solution for photocurrent test. A 300 W Xe lamp (PLS-SXE300, Perfect Light Company, Beijing, China) was used as light source, and the light intensity was 100 mW/cm^2. To prepare the working electrode of TiO_2, 2 mg TiO_2 samples were dispersed into 5 ml deionized water. The suspension was then dip-coated onto a 3 cm × 1 cm fluorine tin oxide (FTO) glass substrates, which were dried at room temperature overnight for next use.

3. Results and discussion

3.1. Morphology and lattice structure

SEM analysis has been carried out to explore the morphology of NP, NR, and NP/NR samples, as shown in Fig. 1. Pure NPs has a spherical morphology with a diameter of 1 μm (Fig. 1a). The SEM image at the high magnification (Fig. 1b) shows that the microsphere is composed of tightly packed small particles (less than 20 nm) and its surface looks rough. Bare NR (Fig. 1c) exhibited the relatively uniform rod-like morphology (a length of ca. 500 nm and a width of ca. 50 nm) and smooth surface. Comparison the size of individual particles and nanorods indicates that NP has the potential to be patched onto the surface of NR. As expected, at the low loading of particles the $NP_{0.25}/NR_{0.75}$ surface was partially covered with particles (Fig. 1d); at the medium loading (i.e., $NP_{0.5}/NR_{0.5}$) nanoparticles were evenly patched on the NR (Fig. 1e), while at the high loading $NP_{0.75}/NR_{0.25}$ surface was fully covered by nanoparticles, some of which tend to aggregate together to form big particles (Fig. 1f). Obviously, we have successfully deposited small particles on the surface of nanorods using a facile one-pot sovolthermal method.

More importantly, the ratio of NP to NR determines the contact, the coverage, and the dispersion of particles on the rods. It should be noted that when patching the NP onto the NR, the NP are small particles instead of the initial microsphere morphology, probably because the NR can serve as a support and block the assembly of single nanoparticle into a microsphere during the solvothermal process. On the other hand, the size of NR slightly decreases when a small amount of NP are loaded (i.e., $NP_{0.25}/NR_{0.75}$). When more NP are introduced (for example, $NP_{0.5}/NR_{0.5}$), the size of NR changed from around 500 nm to 300–400 nm, but NR still maintain the rods-shaped morphology. Since the NP precipitates are tightly attached on the NR, the interaction between them may lead to the size decrease of the NR. The solvothermal treatment and the final calcination processes could also break the long rods down to the short one.

TEM/HRTEM analysis has also been conducted to explore the morphology, particle dispersion and lattice structure. As shown in Fig. 2a and b, the nanorod-shaped NR clearly showed the lattice fringes of 0.48 nm, 0.35 nm, and 0.24 nm, which are corresponding to the anatase phase (002), (101), and (100) facets, respectively [19,20]. In agreement with the literature report [19], NR is mainly enclosed by {100} facets with a growth direction along ⟨001⟩. From Fig. 2c and d one can easily find that the microspheres consist of many small particles (10 nm), and the lattice spacing is 0.35 nm that can be indexed to {101} facets [31]. Regarding the hybrid of $NP_{0.5}/NR_{0.5}$, the TEM image in Fig. 2e confirmed that the nanoparticles were well patched on the surface of NR. The HRTEM image in Fig. 2f clearly showed that $NP_{0.5}/NR_{0.5}$ has both lattice fringes of 0.24 nm for {100} plane, 0.48 nm for {002} plane and 0.35 nm for {101} plane. More importantly, at the interface the NP lattice likely went across the boundary of NR, thus resulting in a strong interaction between them and forming a surface heterojunction of {100}/{101}. As known, TiO_2 NR could contain surface hydroxyls (OH) groups. During the process of grafting TiO_2 NP onto NR, the initial Ti^{4+}-$(OH)_4$ precipitated particles could be bonded with OH groups of NR. The subsequent calcination would lead to the dehydration and the formation of chemical bonds between NP and NR.

3.2. Crystal phase and textural properties

XRD was conducted to identify the crystallinity and phase purity of the resultant materials. As indicated by XRD patterns in Fig. 3a, no matter TiO_2 NP, NR or NP/NR hybrids, all of the samples show the similar diffraction peaks, which can be perfectly indexed to a typical anatase structure (JCPDS card No. 21-1272) without any phase impurity. In addition, all of the samples remained in the similar crystallinity. The ratio of crystal facets were calculated by the Rietveld refinement method (using MAUD software). Fig. 3b and c shows the Rietveld refinement results of $NP_{0.5}/NR_{0.5}$ and NR as examples. It demonstrated two important aspects about the crystal structures of $NP_{0.5}/NR_{0.5}$ and NR: (1) the refinement results (red or pink solid curve) could be fitted nicely with the experimental data (blue dots), and the peak position of the fitting curve also match very well with the standard anatase, which directly proved both of them were composed of pure anatase phase; and (2) the calculated ratio of crystal facet was similar before and after the introduction of NP. For instance, the ratio of (200) facet to (101) facet was 0.382 and 0.376 for $NP_{0.5}/NR_{0.5}$ and NR, respectively. All of the above XRD analyses suggest that NP patched onto NR does not induce neither the transition of crystal phase nor the change of crystal size and crystal facets, because the NP was likely dispersed on the surface of the NR rather than being doped into the lattice.

To further examine the structural characteristics and crystal phase of NP patched NR, Raman spectra have been recorded. As shown in Fig. 3d, all of the TiO_2 samples have nearly identical
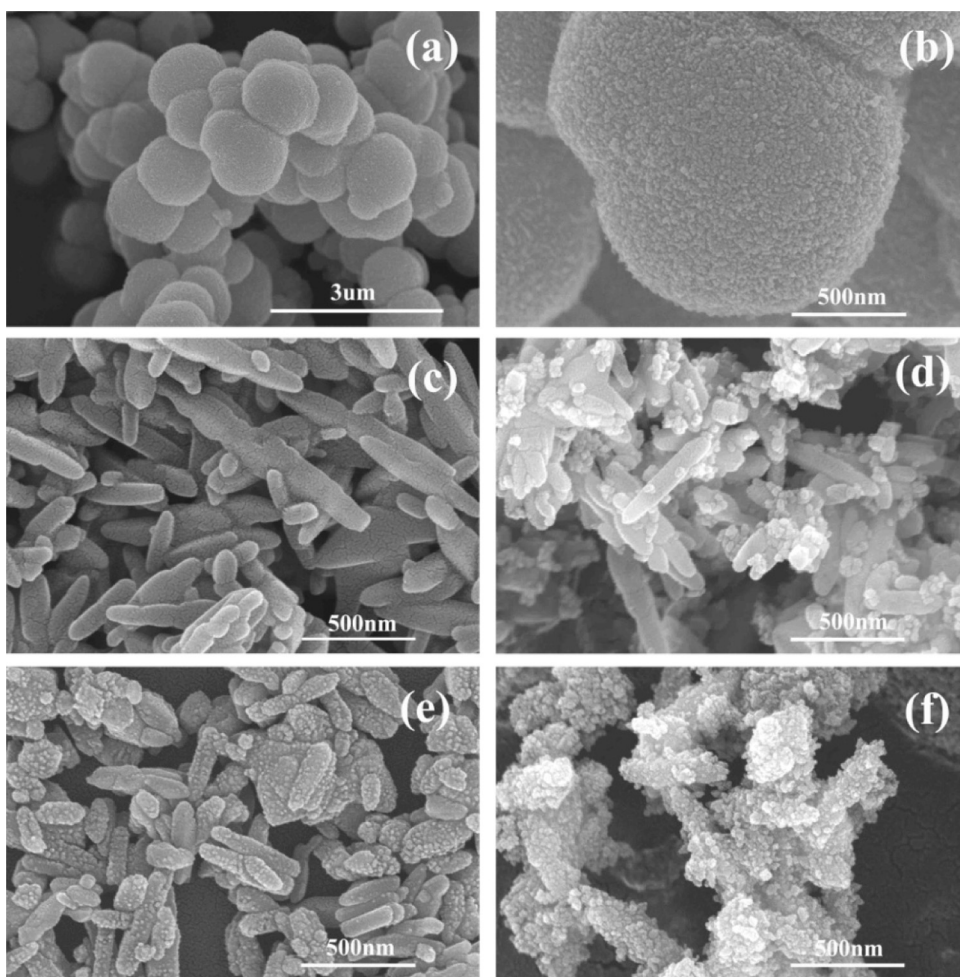
Fig. 1. SEM images for (a and b) NP, (b) NR, (d) $NP_{0.25}/NR_{0.75}$, (e) $NP_{0.5}/NR_{0.5}$, and (f) $NP_{0.75}/NR_{0.25}$ samples.

five Raman-active modes: E_g at 142 cm^{-1}, E_g at 193 cm^{-1}, B1 g at 392 cm^{-1}, A_{1g} at 513 cm^{-1}, and E_g at 640 cm^{-1}, which are attributed to the pure anatase phase [34,38]. No Raman peaks for rutile or brookite phase TiO_2 were observed. In agreement with XRD results, Raman analysis again demonstrate that the NR/NR hybrid remained in the anatase phase without any transformation.

To approach the porosity and textural properties of the samples, we have conducted physical N_2 adsorption analysis. Fig. 4 shows N_2 adsorption–desorption isotherms and the relevant pore size distribution for TiO_2 samples. No any type of hysteresis loop or pore size distribution was observed on NR samples, indicating that there is no mesopores or macrospores in NR. This is likely because NR has a condensed rod-shape and smooth surface, as evidenced by SEM and TEM results. By contrast, NP displayed a typical type IV isotherm with a H_2-type hysteresis loop at the low relative pressure range (0.5–0.8) (Fig. 4a), corresponding to the characteristics of mesoporous structure [24]. The mesopores were likely originated from the space between the packed nanoparticles. In terms of pore size distributions (PSDs), NP shows two sharp PSDs peaks at 3 nm and 7 nm, respectively (Fig. 4b). On the other hand, the NP/NR heterostructures also have type IV isotherms but with a H_3-type hysteresis loop at high relative pressure (0.7–1.0). Moreover, NP/NR samples show broad PSDs peaks centered at 15 nm. Clearly, patching NP onto NR induced the presence of large mesopores on NR, probably because the NP was highly dispersed on the surface of NR, and the space in NP/NR was larger than that in NP. The introduction of NP on NR has also significantly increased the BET specific surface

Table 1
The BET surface area, pore volume, and band gap of NP patched NR with different ratios.

Samples	BET surface area ($m^2\,g^{-1}$)	Pore volume ($cm^3\,g^{-1}$)	Band gap (eV)
NP	72	0.138	3.08
$NP_{0.25}/NR_{0.75}$	86	0.355	3.14
$NP_{0.5}/NR_{0.5}$	44	0.183	3.16
$NP_{0.75}/NR_{0.25}$	43	0.161	3.15
NR	13	0.025	3.18

area and total pore volume of NR (see Table 1). $NP_{0.25}/NR_{0.75}$ has a surface area of 86 m^2/g and pore volume of 0.355 cm^3/g compared to 15 m^2/g and 0.025 cm^3/g for NR. The increase in the surface area and pore volume probably resulted from the small sized and highly dispersed TiO_2 particles (10 nm) and the presence of more mesopores in $NP_{0.25}/NR_{0.75}$. However, the surface area and pore volume decreased to 43 m^2/g and 0.161 cm^3/g when further increasing the amount of NP (i.e. $NP_{0.75}/NR_{0.25}$), likely caused by the aggregation of particles. The above textural properties analyses were well correlated with SEM and TEM results.

3.3. Band gap and chemical state analysis

UV-vis spectra have been recorded to measure the light absorption and the band gap of TiO_2 NP, NR, and NP/NR samples. As shown in Fig. 5a, the band edges of NP, NP/NR and NR were around 412 nm, 403 nm, and 400 nm, respectively. The corresponding band
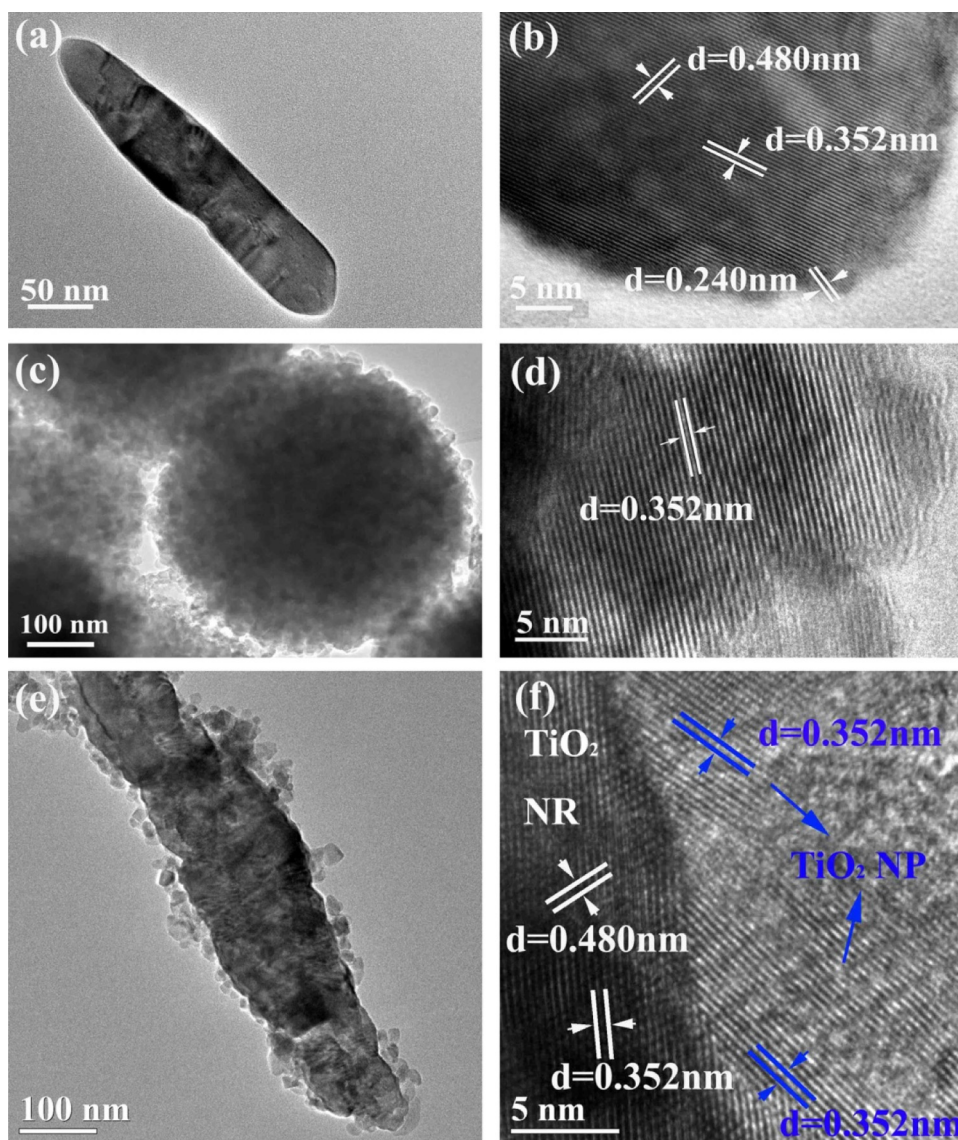
Fig. 2. TEM and HRTEM images for (a and b) NR, (c and d) NP, and (e and f) NP$_{0.5}$/NR$_{0.5}$.

gaps were calculated to be 3.08 eV, 3.16 eV, and 3.18 eV, respectively (according to the Kubelka-Munk function, $(h\nu F(R\infty))^{1/2}$ vs. E$_g$, see Fig. 5b and Table 1). It is noted that even in the same anatase phase, NP shows a red shift in absorption edge and narrowed band gap compared with NR. This is likely because NP has smaller particle size (10 nm) than NR (over 100 nm). When the size is under critical value (20–30 nm), the bulk defects could induce delocalization of molecular orbital in the conduction band edge and create shallow/deep traps in electronic energy [39], in turn causing a red-shift of band edge. Another interesting finding in Fig. 5 is that regardless of changing the ratio of NP to NR, the three NP$_{0.25}$/NR$_{0.75}$, NP$_{0.5}$/NR$_{0.5}$ and NP$_{0.75}$/NR$_{0.25}$ samples have the similar absorption edge, but show a slight red-shift compared with NR. Moreover, the light absorbance of NP$_{0.25}$/NR$_{0.75}$ and NP$_{0.5}$/NR$_{0.5}$ was also enhanced in the UV range (below 360 nm). The results indicate that coupling NP with NR at an appropriate amount could slightly narrow down the band gap of NR, and the mesoporous 0D/1D heterostructure could facilitate the UV light penetration and absorption.

XPS measurement was carried out to probe chemical states of Ti element and to determine the valence band position on the sample surface. As shown in Fig. 6a, NP, NR and NP$_{0.5}$/NR$_{0.5}$ show the

similar and strong Ti 2p3/2 peak at 458.56 eV and Ti 2p1/2 core level at 464.41 eV, which are attributed to the characteristics of Ti^{4+} [29,40,41]. No any other shoulder peaks for Ti^{3+} (457.7 eV) were observed [29], indicating the TiO$_2$ surface was dominantly in +4 state. Fig. 6b shows the valance band (VB) XPS for NP, NR and NP$_{0.5}$NR$_{0.5}$. NP displayed the VB edge at about 2.26 eV below the Fermi energy, while the VB edge of NR was located at 2.42 eV. This VB shift may be caused by the larger particle size and higher energy {100} exposed plane of NR. The VB edge of NP$_{0.5}$/NR$_{0.5}$ hybrid (at 2.30 eV) is very close to NP, indicating that the interaction between NP and NR should induce the alignment of band structure. Because the band gaps of NP and NR are 3.08 eV and 3.18 eV, respectively calculated from the UV–vis spectra, the conduction band (CB) minimum of NP and NR would occur at −0.82 eV and −0.76 eV, respectively. The more negative of the CB minimum of NP, the more reductive electrons will be generated [22].

3.4. Photocatalytic performance analysis

To evaluate the photocatalytic performance of the synthesized TiO$_2$ materials, we first applied the NP/NR hybrids for photocatalytic degradation of methyl orange (MO) under UV–vis light
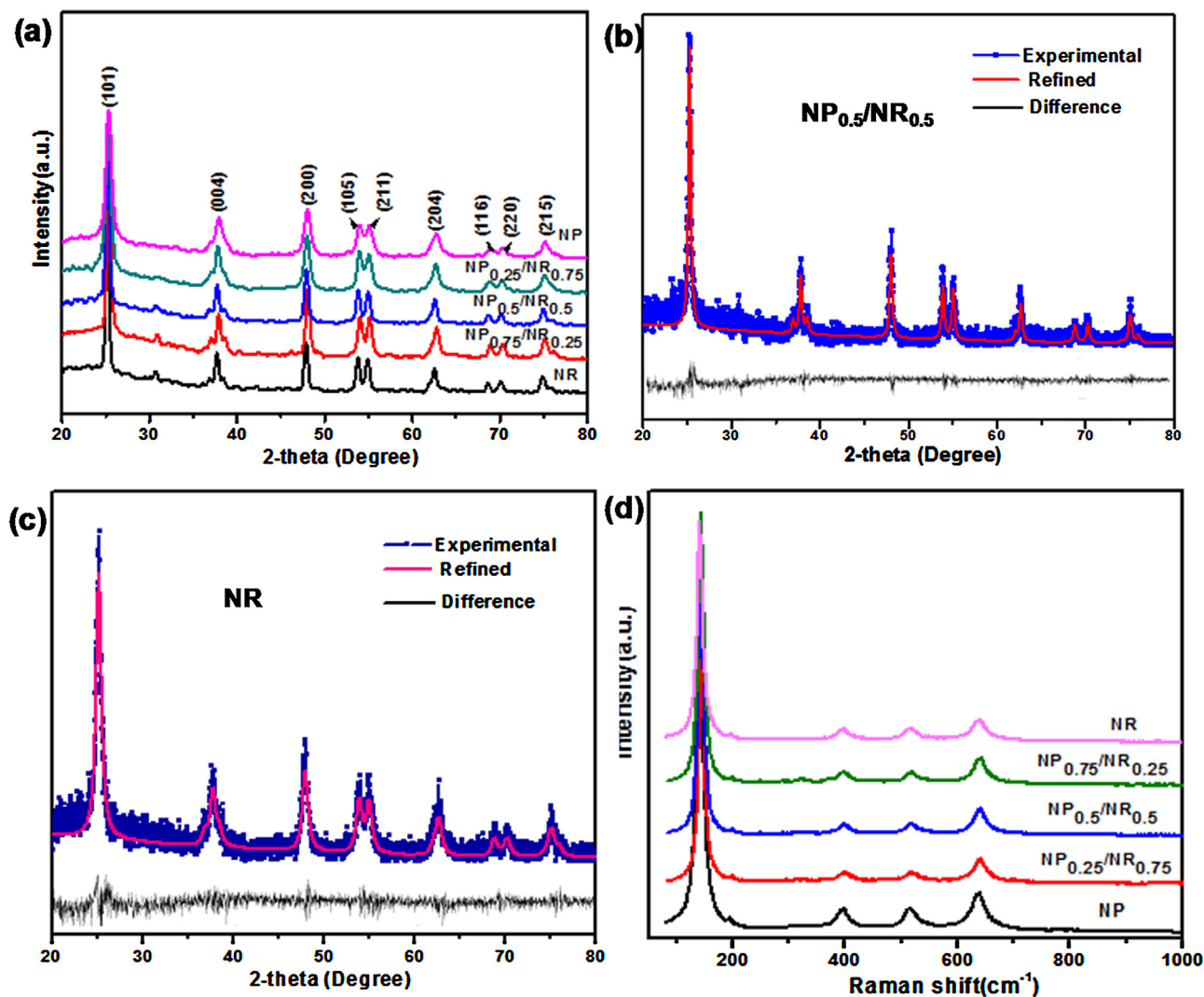
Fig. 3. (a) XRD patterns for NP, NR and NP/NR samples, (b and c) rietveld refinement results for $NP_{0.5}/NR_{0.5}$ and NR, and (d) Raman spectra for NP, NR and NP/NR samples. (For interpretation of the references to color in the text, the reader is referred to the web version of this article.)
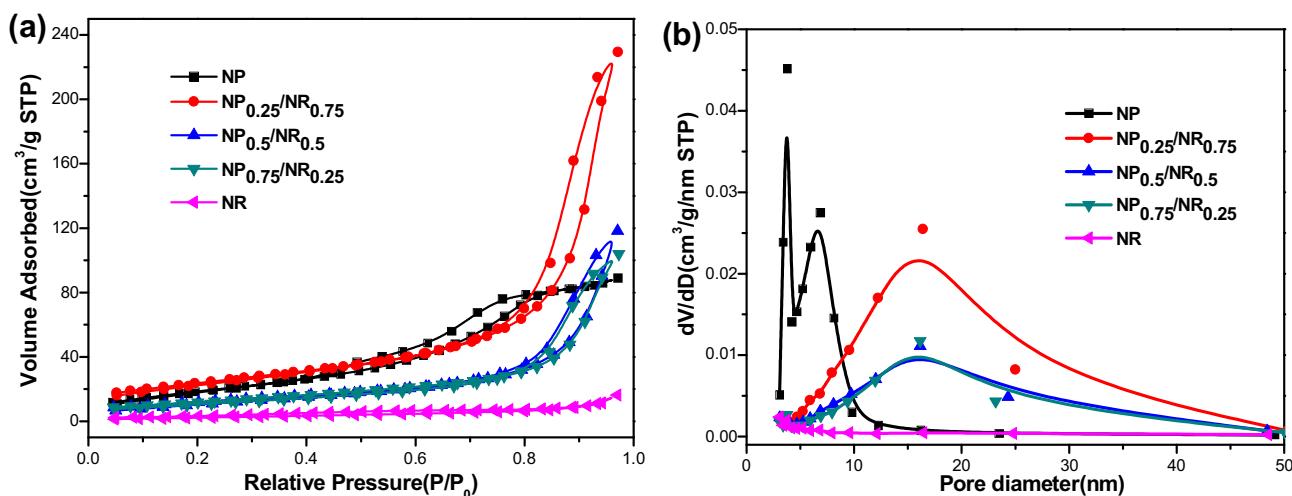

Fig. 4. (a) N_2 adsorption–desorption isotherms of NP patched NR samples with different ratios, and (b) the corresponding pore-size distribution using the BJH model.

irradiation. We calculated the concentration ratio (C_t/C_0) of MO and plotted it against photo-irradiation time. Fig. 7a compares the activity of NP, NR, and NP/NR samples. From Fig. 7a, one can clearly find that the complete degradation of MO over NR requires 120 min, while NP just needs 60 min to remove organics by 100%. The higher activity of NP than NR could result from the smaller par-
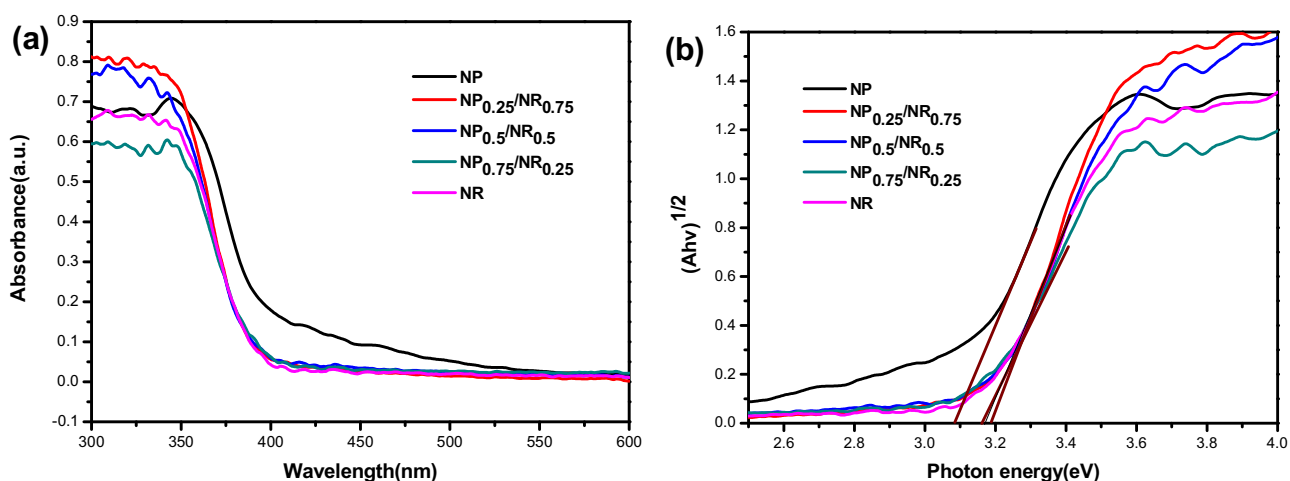
Fig. 5. (a) UV–vis spectra and (b) the band gap for NP patched NR with different ratios.
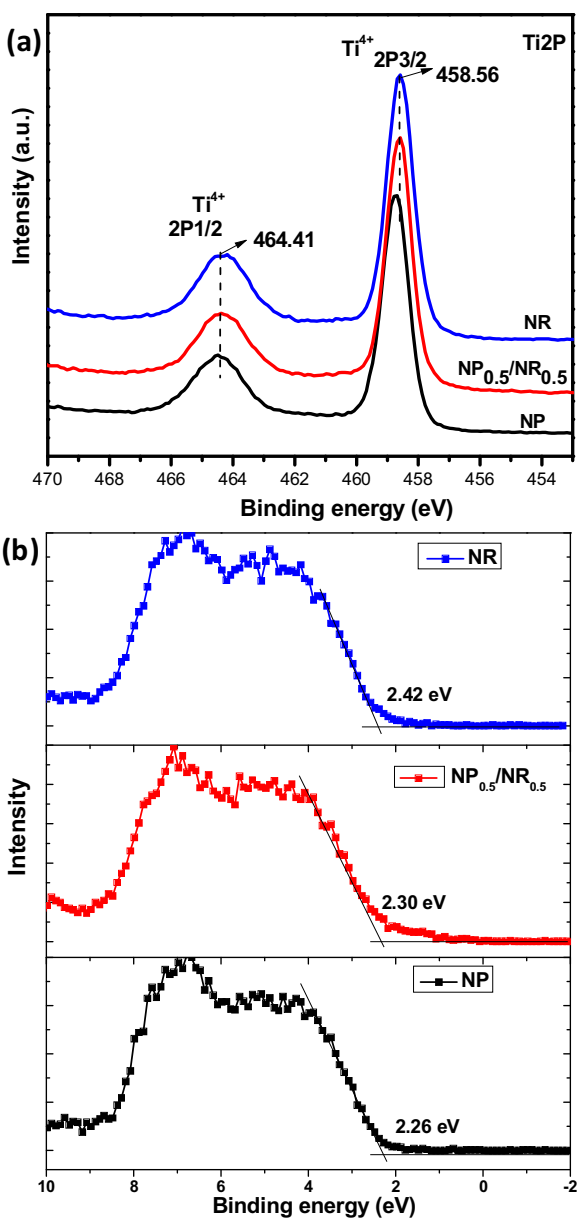

Fig. 6. (a) Ti 2p and (b) valence band XPS spectra for NP, NR and $NP_{0.5}/NR_{0.5}$.

ticle size, larger surface area and pore volume that could provide more active sites and full contact with organic molecules. More importantly, patching NP onto NR significantly enhanced the efficiency of NR, and the resulting NP/NR was even more active than NP. At the low loading, $NP_{0.5}/NR_{0.5}$ demonstrated the highest activity and removed MO completely within 30 min. Further increasing the amount of NP (i.e., $NP_{0.75}/NR_{0.25}$) resulted in the decrease of photodegradation efficiency. To further understand the difference among them, we calculated the reaction rate constant by plotting the $\ln(C_0/C_t)$ versus time, assuming that all oxidation processes follow pseudo-first-order kinetics. As shown in Fig. 7b, the reaction rate constants in degradation of MO are 0.0464 for NP, 0.0760 for $NP_{0.25}/NR_{0.75}$, 0.0832 for $NP_{0.5}/NR_{0.5}$, 0.0315 for $NP_{0.75}/NR_{0.25}$, and 0.0208 for NR. Obviously, $NP_{0.5}/NR_{0.5}$ has the highest rate constant. Hence, the ratio of NP to NR is an important factor to govern the efficiency and reaction rate. In this work $NP_{0.5}/NR_{0.5}$ has the optimum ratio.

Since $NP_{0.5}/NR_{0.5}$ is most active among the samples, we further performed its cycling capability and the ability to degrade other organic compounds to evaluate its superiority. As shown in Fig. 7c, even after 6 cycles, $NP_{0.5}/NR_{0.5}$ still maintained over 98% degradation efficiency for MO removal. In Fig. 7d, $NP_{0.5}/NR_{0.5}$ also shows excellent capability to quickly degrade other four types of organics such as methyl blue, rhodamine B, malachite Green and bisphenol A. Again, the outstanding cycling performance and the strong ability to decompose multiple organics confirm our original hypothesis that the NP-patched-NR hybrid has great advantages and potentials for water treatment.

We further extend the application of our NP/NR materials from photo-oxidation to photo-reduction, i.e., H_2 production from water splitting. As shown in Fig. 7e, NP has the H_2 production rate of 15 μmol/g/h, nearly three times higher than NR (4 μmol/g/h). When loading a small amount of NP on NR (i.e., $NP_{0.25}/NR_{0.75}$), the H_2 production rate was slightly enhanced by 25%. More impressively, the highest H_2 production rate was achieved on $NP_{0.5}/NR_{0.5}$ (53 μmol/g/h), 12 times and over 2.5 times higher than NR and NP, respectively. However, further increasing the amount of NP on NR (i.e., $NP_{0.75}/NR_{0.25}$) limited the enhancement of H_2 production. Again, the H_2 evolution performance demonstrated the superiority and multi-functional capability of $NP_{0.5}/NR_{0.5}$ heterostructure.

By comparing the data Fig. 7a and e, we found that the overall activity trend in the photo-degradation of MO is same as water splitting to H_2, i.e., $NP_{0.5}/NR_{0.5} > NP_{0.25}/NR_{0.75} > NP > NP_{0.75}/NR_{0.25} > NR$. Even NR has higher surface energy exposed {100} plane than NP with {101}
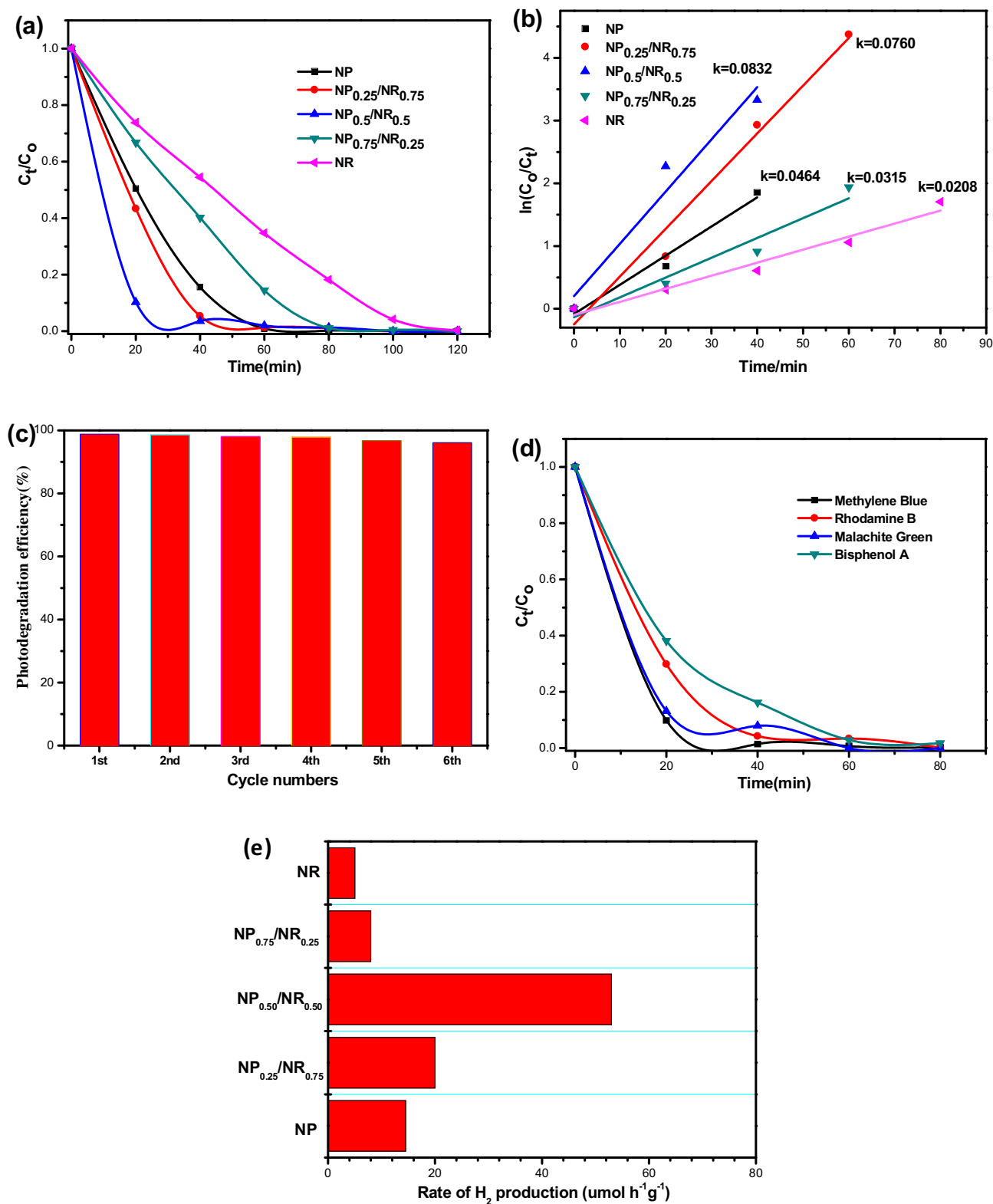
Fig. 7. (a) Photocatalytic degradation of methyl Orange (MO) by NP patched NR with different ratios under UV–vis irradiation, (b) the reaction rate constant in photocatalytic degradation of MO, (c) cycling performance of the $NP_{0.5}/NR_{0.5}$ for MO degradation, (d) the photodegradation of methylene blue, rhodamine B, malachite green and bisphenol A by $NP_{0.5}/NR_{0.5}$ photocatalyst under UV–vis irradiation (catalyst dosage = 1 mg/ml, initial pollutants concentration = 10 ppm, near neutral pH), and (e) the H_2 production rate from photocatalytic water splitting over NP patched NR with different ratios under UV–vis irradiation. (For interpretation of the references to colour in this figure legend, the reader is referred to the web version of this article.)

plane, the activity of NR was lower than NP. This is likely because NP has much higher surface area and pore volume than NR. Compared to the non-porous structure of NR, the mesopores in NP

may facilitate the molecules transport and diffusion. Hence, there is a trade-off between the exposed plane and textural properties. Compared with individual NP and NR, the hybridization of NP onto
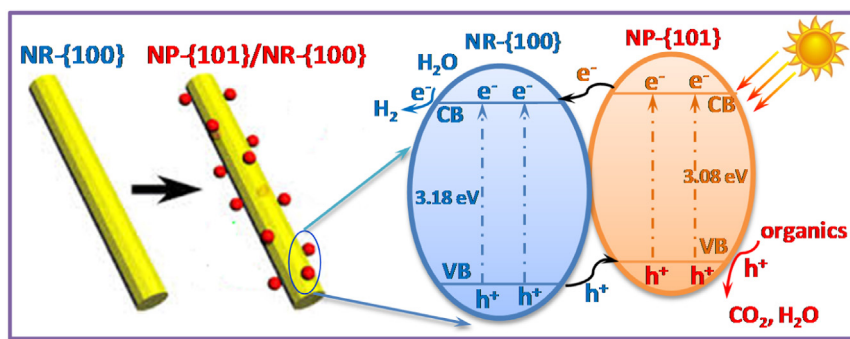
Fig. 8. The scheme of the possible heterostructure of NP-{101}/NR-{100} and the transfer pathway of charge carriers on the NP-{101}/NR-{100} surface heterjunction.

NR has boosted the photocatalytic activity, depending on the ratio of NP to NR. $NP_{0.25}/NR_{0.75}$ has the largest surface area and pore volume, but its activity was lower than the $NP_{0.5}/NR_{0.5}$. The activity of $NP_{0.75}/NR_{0.25}$ was also inferior to $NP_{0.5}/NR_{0.5}$, possibly because the aggregation of particles weakened the interaction between NP and NR and decreased the charger separation efficiency (see the photocurrent results described later in this paper). By correlating with the results of TEM/HRTEM, XPS VB measurement and UV–vis band gap analysis, the superior activity of $NP_{0.5}/NR_{0.5}$ could be primarily attributed to the good dispersion of particles and the formed surface heterojunction. The two factors may facilitate the separation and transfer of charge carriers. As mentioned above in Fig. 6b, the VB edge of NR is more positive than that of NP. Since the band gap of NP was smaller than NR (see Fig. 4b), the calculated CB edge of NP was more negative than NR. Clearly, the band positions of NP and NR are mismatched. In addition, because NP {101} and NR {100} exposed facets are closely contacted (see Fig. 2f), it is very likely to form a {101}/{100} surface heterojunction.

Fig. 8 shows the possible heterostructure of NP-{101}/NR-{100}. In such a heterojunction, the photo-excited electrons migrate from the more reductive NP-{101} CB to NR-{100} CB, while the holes are transferred from the more oxidative NR-{100} VB to NP-{101} VB at a low energy level. The separated electrons can reduce H_2O to H_2, and the holes can oxidize the organic compounds to CO_2 and H_2O. As a consequence, the enhanced charge separation and transfer induces the superior activity of the heterostructured NP/NR compared with pure NR and NP. To confirm this deduction, we measured the photocurrent of the NR and NR/NP samples. As shown in Fig. 9, patching NP on NR remarkably enhanced the photocurrent compared with NR. Especially $NP_{0.5}/NR_{0.5}$ has the highest photocurrent of 4.0–4.5 $\mu A/cm^2$, over 4 times higher than NR. On the other hand, further increasing the loading amount of NP resulted in a decrease in the photocurrent on $NP_{0.75}/NR_{0.25}$ but still higher than NR, indicating $NP_{0.75}/NR_{0.25}$ is inferior to $NP_{0.5}/NR_{0.5}$ to transfer electrons. The photocurrent measurement results demonstrated that the NP/NR heterojunction indeed facilitated the charge carriers separation and transfer, which correlated very well with the photocatalytic performance.

4. Conclusions

In this work we have used a simple hydrothermal method to fabricate a novel heterostructure of TiO_2 nanoparticles (NP) patched nanorods (NR) with a tuneable ratio. NP and NR have the dominated {101} and {100} exposed plane, respectively, while surface heterojunction of {100}/{101} is formed in NP/NR hybrid because of their close contact and band structure alignment. Compared with NP and NR alone, the NP/NR heterostructure showed superior activities in the photodegradation of multiple organic compounds and water splitting to H_2, mainly due to the enhanced charge separation
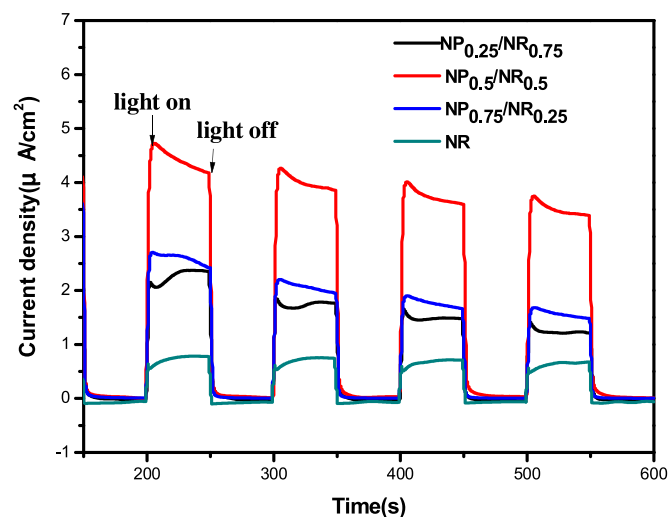

Fig. 9. Photocurrent density of NR and NP/NR samples during the UV–vis light on/off cycles.

and transfer in the {100}/{101} surface junction. The ratio of NP to NR is an important factor to affect the NP dispersion, porosity, the contact between NP and NR, the {100}/{101} fraction and charge transfer, thus governing the photocatalytic performance of NP/NR. The optimal ratio of NP to NR was determined to be 50:50. The findings in this work not only fundamentally interpret the relationships of materials structure-performance, but also provide a new insight into the design and fabrication of advanced photocatalytic materials for energy and environmental application.

Acknowledgements

References

[1] J. Tian, Z. Zhao, A. Kumar, R.I. Boughton, H. Liu, Recent progress in design, synthesis, and applications of one-dimensional TiO₂ nanostructured surface heterostructures: a review, Chem. Soc. Rev. 43 (2014) 6920–6937.
[2] W.-J. Ong, L.-L. Tan, S.-P. Chai, S.-T. Yong, A.R. Mohamed, Facet-dependent photocatalytic properties of TiO₂-based composites for energy conversion and environmental remediation, ChemSusChem 7 (2014) 690–719.
[3] J. Schneider, M. Matsuoka, M. Takeuchi, J. Zhang, Y. Horiuchi, M. Anpo, D.W. Bahnemann, Understanding TiO₂ photocatalysis: mechanisms and materials, Chem. Rev. 114 (2014) 9919–9986.

[4] X. Wang, Z. Li, J. Shi, Y. Yu, One-dimensional titanium dioxide nanomaterials: nanowires, nanorods, and nanobelts, Chem. Rev. 114 (2014) 9346–9384.

[5] J. Mao, L. Ye, K. Li, X. Zhang, J. Liu, T. Peng, L. Zan, Pt-loading reverses the photocatalytic activity order of anatase TiO_2 {001} and {010} facets for photoreduction of CO_2 to CH_4, Appl. Catal. B-Environ. 144 (2014) 855–862.

[6] V.P. Indrakanti, H.H. Schobert, J.D. Kubicki, Quantum mechanical modeling of CO_2 interactions with irradiated stoichiometric and oxygen-deficient anatase TiO_2 surfaces: implications for the photocatalytic reduction of CO_2, Energy Fuels 23 (2009) 5247–5256.

[7] Z. Zhao, J. Fan, J. Wang, R. Li, Effect of heating temperature on photocatalytic reduction of CO2 by N-TiO2 nanotube catalyst, Catal. Commun. 21 (2012) 32–37.

[8] L.-F. Chiang, R.-a. Doong, Cu-TiO2 nanorods with enhanced ultraviolet- and visible-light photoactivity for bisphenol A degradation, J. Hazard. Mater. 277 (2014) 84–92.

[9] S. Zhou, Y. Liu, J. Li, Y. Wang, G. Jiang, Z. Zhao, D. Wang, A. Duan, J. Liu, Y. Wei, Facile in situ synthesis of graphitic carbon nitride (g-C_3N_4)-N-TiO_2 heterojunction as an efficient photocatalyst for the selective photoreduction of CO_2 to CO, Appl. Catal. B-Environ. 158 (2014) 20–29.

[10] R. Asahi, T. Morikawa, H. Irie, T. Ohwaki, Nitrogen-doped titanium dioxide as visible-light-sensitive photocatalyst: designs, developments, and prospects, Chem. Rev. 114 (2014) 9824–9852.

[11] M.-V. Sofianou, M. Tassi, V. Psycharis, N. Boukos, S. Thanos, T. Vaimakis, J. Yu, C. Trapalis, Solvothermal synthesis and photocatalytic performance of Mn^{4+}-doped anatase nanoplates with exposed {001} facets, Appl. Catal. B-Environ. 162 (2015) 27–33.

[12] X. Li, H. Liu, D. Luo, J. Li, Y. Huang, H. Li, Y. Fang, Y. Xu, L. Zhu, Adsorption of CO_2 on heterostructure CdS(Bi_2S_3)/TiO_2 nanotube photocatalysts and their photocatalytic activities in the reduction of CO_2 to methanol under visible light irradiation, Chem. Eng. J. 180 (2012) 151–158.

[13] C. Wang, R.L. Thompson, J. Baltrus, C. Matranga, Visible light photoreduction of CO_2 using CdSe/Pt/TiO_2 heterostructured catalysts, J. Phys. Chem. Lett. 1 (2010) 48–53.

[14] H. Li, X. Cui, A hydrothermal route for constructing reduced graphene oxide/TiO2 nanocomposites: enhanced photocatalytic activity for hydrogen evolution, Int. J. Hydrogen Energy 39 (2014) 19877–19886.

[15] Y.T. Liang, B.K. Vijayan, O. Lyandres, K.A. Gray, M.C. Hersam, Effect of dimensionality on the photocatalytic behavior of carbon-titania nanosheet composites: charge transfer at nanomaterial interfaces, J. Phys. Chem. Lett. 3 (2012) 1760–1765.

[16] W.-J. Ong, L.-L. Tan, S.-P. Chai, S.-T. Yong, A.R. Mohamed, Self-assembly of nitrogen-doped TiO_2 with exposed {001} facets on a graphene scaffold as photo-active hybrid nanostructures for reduction of carbon dioxide to methane, Nano Res. 7 (2014) 1528–1547.

[17] G. Liu, H.G. Yang, J. Pan, Y.Q. Yang, G.Q. Lu, H.-M. Cheng, Titanium dioxide crystals with tailored facets, Chem. Rev. 114 (2014) 9559–9612.

[18] L. Liu, X. Chen, Titanium dioxide nanomaterials: self-structural modifications, Chem. Rev. 114 (2014) 9890–9918.

[19] J. Li, D. Xu, Tetragonal faceted-nanorods of anatase TiO_2 single crystals with a large percentage of active {100} facets, Chem. Commun. 46 (2010) 2301–2303.

[20] L. Ye, J. Mao, J. Liu, Z. Jiang, T. Peng, L. Zan, Synthesis of anatase TiO_2 nanocrystals with {101}, {001} or {010} single facets of 90% level exposure and liquid-phase photocatalytic reduction and oxidation activity orders, J. Mater. Chem. A 1 (2013) 10532–10537.

[21] J. Long, H. Chang, Q. Gu, J. Xu, L. Fan, S. Wang, Y. Zhou, W. Wei, L. Huang, X. Wang, P. Liu, W. Huang, Gold-plasmon enhanced solar-to-hydrogen conversion on the {001} facets of anatase TiO_2 nanosheets, Energy Environ. Sci. 7 (2014) 973–977.

[22] H. Xu, S. Ouyang, P. Li, T. Kako, J. Ye, High-active anatase TiO_2 nanosheets exposed with 95% {100} facets toward efficient H-2 evolution and CO_2 photoreduction, ACS Appl. Mater. Interfaces 5 (2013) 1348–1354.

[23] Y. Zhang, M. Shang, Y. Mi, T. Xia, P. Wallenmeyer, J. Murowchick, L. Dong, Q. Zhang, X. Chen, Influence of the amount of hydrogen fluoride on the formation of (001)-faceted titanium dioxide nanosheets and their photocatalytic hydrogen generation performance, ChemPlusChem 79 (2014) 1159–1166.

[24] L. Liu, H. Zhao, J.M. Andino, Y. Li, Photocatalytic CO_2 reduction with H_2O on TiO_2 nanocrystals: comparison of anatase, rutile, and brookite polymorphs and exploration of surface chemistry, ACS Catal. 2 (2012) 1817–1828.

[25] G. Zhang, Q. Xiong, W. Xu, S. Guo, Synthesis of bicrystalline TiO_2 supported sepiolite fibers and their photocatalytic activity for degradation of gaseous formaldehyde, Appl. Clay Sci. 102 (2014) 231–237.

[26] L. Liu, D.T. Pitts, H. Zhao, C. Zhao, Y. Li, Silver-incorporated bicrystalline (anatase/brookite) TiO_2 microspheres for CO_2 photoreduction with water in the presence of methanol, Appl. Catal. A: Gen. 467 (2013) 474–482.

[27] B. Tian, C. Li, J. Zhang, One-step preparation, characterization and visible-light photocatalytic activity of Cr-doped TiO_2 with anatase and rutile bicrystalline phases, Chem. Eng. J. 191 (2012) 402–409.

[28] K.L. Schulte, P.A. DeSario, K.A. Gray, Effect of crystal phase composition on the reductive and oxidative abilities of TiO_2 nanotubes under UV and visible light, Appl. Catal. B-Environ. 97 (2010) 354–360.

[29] L.R. Grabstanowicz, S. Gao, T. Li, R.M. Rickard, T. Rajh, D.-J. Liu, T. Xu, Facile oxidative conversion of TiH_2 to high-concentration Ti^{3+}-self-doped rutile TiO_2 with visible-light photoactivity, Inorg. Chem. 52 (2013) 3884–3890.

[30] N. Roy, Y. Sohn, D. Pradhan, Synergy of low-energy {101} and high-energy {001} TiO_2 crystal facets for enhanced photocatalysis, Acs Nano 7 (2013) 2532–2540.

[31] J. Yu, J. Low, W. Xiao, P. Zhou, M. Jaroniec, Enhanced photocatalytic CO_2-reduction activity of anatase TiO_2 by coexposed {001} and {101} facets, J. Am. Chem. Soc. 136 (2014) 8839–8842.

[32] Z. He, L. Wen, D. Wang, Y. Xue, Q. Lu, C. Wu, J. Chen, S. Song, Photocatalytic reduction of CO_2 in aqueous solution on surface-fluorinated anatase TiO_2 nanosheets with exposed {001} facets, Energy Fuels 28 (2014) 3982–3993.

[33] M.-Y. Xing, B.-X. Yang, H. Yu, B.-Z. Tian, S. Bagwasi, J. Zhang, X.-Q. Gongs, Enhanced photocatalysis by Au nanoparticle loading on TiO_2 single-crystal (001) and (110) facets, J. Phys. Chem. Lett. 4 (2013) 3910–3917.

[34] B. Wu, C. Guo, N. Zheng, Z. Xie, G.D. Stucky, Nonaqueous production of nanostructured anatase with high-energy facets, J. Am. Chem. Soc. 130 (2008) 17563–17567.

[35] M. Calatayud, C. Minot, Effect of relaxation on structure and reactivity of anatase (100) and (001) surfaces, Surf. Sci. 552 (2004) 169–179.

[36] J.S. Chen, Y.L. Tan, C.M. Li, Y.L. Cheah, D. Luan, S. Madhavi, F.Y.C. Boey, L.A. Archer, X.W. Lou, Constructing hierarchical spheres from large ultrathin anatase TiO_2 nanosheets with nearly 100% exposed (001) facets for fast reversible lithium storage, J. Am. Chem. Soc. 132 (2010) 6124–6130.

[37] F. Liu, Y. Xie, C. Yu, X. Liu, Y. Dai, L. Liu, Y. Ling, Novel hybrid Sr-doped TiO_2/magnetic $Ni_{0.6}Zn_{0.4}Fe_2O_4$ for enhanced separation and photodegradation of organics under visible light, RSC Adv. 5 (2015) 24056–24063.

[38] H. Zhao, L. Liu, J.M. Andino, Y. Li, Bicrystalline TiO_2 with controllable anatase-brookite phase content for enhanced CO_2 photoreduction to fuels, J. Mater. Chem. A 1 (2013) 8209–8216.

[39] H. Lin, C.P. Huang, W. Li, C. Ni, S.I. Shah, Y.-H. Tseng, Size dependency of nanocrystalline TiO_2 on its optical property and photocatalytic reactivity exemplified by 2-chlorophenol, Appl. Catal. B-Environ. 68 (2006) 1–11.

[40] J. Wang, P. Zhang, X. Li, J. Zhu, H. Li, Synchronical pollutant degradation and H-2 production on a Ti^{3+}-doped TiO_2 visible photocatalyst with dominant (001) facets, Appl. Catal. B-Environ. 134 (2013) 198–204.

[41] L. Liu, F. Gao, H. Zhao, Y. Li, Tailoring Cu valence and oxygen vacancy in Cu/TiO_2 catalysts for enhanced CO_2 photoreduction efficiency, Appl. Catal. B-Environ. 134 (2013) 349–358.